Prism Computational Sciences, Inc.
455 Science Drive, Suite 140
Madison, WI 53711

Development of Spectral and Atomic Models for Diagnosing Energetic Particle Characteristics in Fast Ignition Experiments

STTR Phase II Final Report

Grant No.: DE-FG02-05ER86258
Program Manager: Francis Thio

J. J. MacFarlane*, I. E. Golovkin, P. R. Woodruff
Prism Computational Sciences, Inc.

D. R. Welch, C. Thoma, T. A. Hughes
Voss Scientific, LLC

P. Hakel, R. C. Mancini
University of Nevada - Reno

PCS-R-105

August 2009

* Contractor Point of Contact (Tel. 608-280-9182; Email: jjm@prism-cs.com)

Contents

1. Executive Summary

This Final Report summarizes work performed under DOE STTR Phase II Grant No. DE-FG02-05ER86258 during the project period from August 2006 to August 2009. The project, "Development of Spectral and Atomic Models for Diagnosing Energetic Particle Characteristics in Fast Ignition Experiments," was led by Prism Computational Sciences (Madison, WI), and involved collaboration with subcontractors University of Nevada-Reno and Voss Scientific (Albuquerque, NM).

In this project, we have:

- Developed and implemented a multi-dimensional, multi-frequency radiation transport model in the LSP hybrid fluid-PIC (particle-in-cell) code [1,2].
- Updated the LSP code to support the use of accurate equation-of-state (EOS) tables generated by Prism's PROPACEOS [3] code to compute more accurate temperatures in high energy density physics (HEDP) plasmas.
- Updated LSP to support the use of Prism's multi-frequency opacity tables.
- Generated equation of state and opacity data for LSP simulations for several materials being used in plasma jet experimental studies.
- Developed and implemented parallel processing techniques for the radiation physics algorithms in LSP.
- Benchmarked the new radiation transport and radiation physics algorithms in LSP and compared simulation results with analytic solutions and results from numerical radiation-hydrodynamics calculations.
- Performed simulations using Prism radiation physics codes to address issues related to radiative cooling and ionization dynamics in plasma jet experiments.
- Performed simulations to study the effects of radiation transport and radiation losses due to electrode contaminants in plasma jet experiments.
- Updated the LSP code to generate output using NetCDF to provide a better, more flexible interface to SPECT3D [4] in order to post-process LSP output.
- Updated the SPECT3D code to better support the post-processing of large-scale 2-D and 3-D datasets generated by simulation codes such as LSP.
- Updated atomic physics modeling to provide for more comprehensive and accurate atomic databases that feed into the radiation physics modeling (spectral simulations and opacity tables).
- Developed polarization spectroscopy modeling techniques suitable for diagnosing energetic particle characteristics in HEDP experiments.

A description of these items is provided in this report.

The above efforts lay the groundwork for utilizing the LSP and SPECT3D codes in providing simulation support for DOE-sponsored HEDP experiments, such as plasma jet and fast ignition physics experiments. We believe that taken together, the LSP and SPECT3D codes have unique capabilities for advancing our understanding of the physics of these HEDP plasmas.

Technical and Administrative Issues

Based on conversations early in this project with our DOE program manager, Dr. Francis Thio, our efforts emphasized developing radiation physics and atomic modeling capabilities that can be utilized in the LSP PIC code, and performing radiation physics studies for plasma jets. A relatively minor component focused on the development of methods to diagnose energetic particle characteristics in short-pulse laser experiments related to fast ignition physics.

The period of performance for the grant was extended by one year to August 2009 with a one-year no-cost extension, at the request of subcontractor University of Nevada-Reno.

2. Implementation of Accurate Equation of State Modeling in LSP

Energy Equation Modeling

In this section, we describe work to improve the equation-of-state (EOS) modeling in the LSP PIC code. Hybrid codes such as LSP have shown the ability to model important kinetic features in plasma jets [5] and in fast ignition experiments [6]. To relax timestep and grid-size constraints imposed by the bulk electron density, the bulk electrons are modeled as a fluid. Prior to this work, these codes used an ideal gas model for the fluid electrons. Thus, the electron fluid energy equation in LSP was:

$$\frac{3}{2} n_e \frac{dT_e}{dt} = -n_e T_e \nabla . \mathbf{v}_e + \nabla . \kappa_e \nabla T_e + \sum_{i=1}^{N_s} \frac{3 m_e n_e}{m_i \tau_{ei}} \left(T_i - T_e \right) + Q_e \tag{2.1}$$

where N_s is the number of ion species. The terms on the right-hand side are:

- Energy loss due to adiabatic decrease in the density.
- Energy gained through thermal conduction from the surrounding fluid. In the absence of a magnetic field, the thermal conductivity κ_e is given by the Spitzer expression:

$$\kappa_e = 3.16 \frac{n_e T_e \tau_{ei}}{m_e} \tag{2.2}$$

- Collisional energy exchange with ions on the electron-ion collision timescale τ_{ei}.
- Ohmic heating of the electrons, using the Braginskii expression:

$$Q_e = \sum_{i=1}^{N_s} \frac{n_e m_e}{\tau_{ei}} \left(u_{i\|}^2 + \frac{u_{i\perp}^2}{1.96} \right) \tag{2.3}$$

  where $\mathbf{u}_i$ is the relative drift velocity between the electrons and the i^{th} ion species. The "thermoelectric" term is not included in this expression.
- Other losses, *e.g.*, electromagnetic radiation and inelastic collisions with neutral atoms.

In writing Eq. (2.1), we have closed the hierarchy of fluid equations by assuming an ideal gas equation-of-state ($p = n_e T_e$) for the electrons. This approximation does not include the energy going into ionization and excitation, and in addition, at high densities, the electron potential energy, and quantum-statistical effects can significantly modify the relation between the internal energy, pressure, and temperature. Also, for plasmas where the ions are not fully stripped, the average ionization state, $\overline{Z}$, is needed to compute the free-electron density, and for correct ion dynamics.

To overcome these deficiencies, we have modified the LSP code to use tabulated equation-of-state tables developed by Prism. The tables are based on a hybrid model, which includes a QEOS-type model [7] in the strongly-coupled plasma regime (high densities and low temperatures) and an isolated atom, multi-level collisional-radiative

model in the weakly-coupled regime. This provides smoothly-varying values of thermodynamic quantities, such as electron and ion energy and pressure, over a broad range of densities and temperatures.

For the electrons, the equation of energy conservation, Eq. (2.1), is replaced by:

$$\rho \frac{d\varepsilon_e}{dt} = -p_e \nabla.\mathbf{v} + \nabla.\kappa_e \nabla T_e + \frac{3m_e n_e}{m_i \tau_{ei}}\left(T_i - T_e\right) + Q_e \tag{2.4}$$

where ε_e is the electron-gas energy per unit mass (specific internal energy) and p_e is the electron pressure. The sum over different ion charge states is replaced by a single average-atom ion species.

The new algorithm proceeds as follows:

- Perform a collisionless velocity-advance for electrons and ions. This takes care of advection terms in the fluid-electron equations.
- If the ions are being treated as a kinetic species, apply ion-ion collisions.
- Compute the electron-ion collisional effects using the Braginskii expressions for the frictional force and the electron-ion energy exchange:

$$\mathbf{F}_i = -\frac{n_e{}^2 e^2 (\mathbf{v}_e - \mathbf{v}_i)}{\sigma} - 0.71 n_e \nabla T_e,\ \mathbf{F}_e = -\mathbf{F}_i \tag{2.5}$$

$$W_i = \frac{3m_e n_e}{m_i \tau_{ie}}\left(T_i - T_e\right),\ W_e = -W_i + \frac{\mathbf{j}_e \cdot \mathbf{F}_i}{n_e e} \tag{2.6}$$

  Equation (2.4) includes the electrothermal term. The conductivity σ can be calculated from the LMD [8] model.
- Update the particle momenta, ion thermal energy, and electron internal energy using Eqs. (2.4) - (2.6).
- Update particle positions, and compute densities and temperatures at the grid nodes.
- Use the EOS tables to obtain the pressure and $\bar{Z}$ values at the grid nodes.
- Scale the individual ion and electron charge-weights in each cell to be consistent with $\bar{Z}$.

At the end of this cycle, an electron pressure and ion charge-state are computed consistent with the EOS tables, and these are used in the next timestep.

Inclusion of Thermoelectric Term

The temperature/energy equation in LSP has been further generalized to include the thermoelectric term (whereby a temperature gradient generates an electric field), and to use transport coefficients which are functions of the Hall parameter, following Braginskii's treatment [9]. In 1-D, the electron temperature equation can now be written as:

$$\frac{\partial T_e}{\partial t} = -v_{ex}\frac{\partial T_e}{\partial x} + \frac{1}{n_e}\frac{\partial}{\partial x}\left[\frac{2\kappa_\perp}{3}\frac{\partial T_e}{\partial x_e} - 2GT_e\right] + \frac{T_e}{n_e}\frac{\partial G}{\partial x} + \frac{2}{3n_e}\eta J_y^2 + \sum_{i=1}^{N_s}\frac{2m_e}{m_i\tau_{ei}}\left(T_i - T_e\right) + Q_e \quad (2.7)$$

where $\kappa_\perp$ is the thermal conductivity transverse to the magnetic field, the plasma resistivity is given by:

$$\eta = \frac{\alpha_\perp}{n_e^2 e^2}, \qquad \text{and} \qquad G = \left(\frac{2\beta_\wedge}{3n_e}\right)\frac{J_y}{e}.$$

The three coefficients $\kappa_\perp$, $\alpha_\perp$, $\beta_\wedge$ are written as functions of the Hall parameter, x:

$$\frac{\alpha_\perp\sigma_0}{n_e^2e^2} = 1 - \frac{\alpha_0 + \alpha_1 x^2}{\Delta},\ \frac{\beta_\wedge}{n_e} = \frac{x(\beta_0 + \beta_1 x^2)}{\Delta},\ \frac{\kappa_\perp}{\kappa_0} = \frac{\gamma_0 + \gamma_1 x^2}{\Delta}, \quad (2.8)$$

where

$$\Delta = \delta_0 + \delta_1 x^2 + x^4,\ \sigma_0 = \frac{n_e e^2}{m_e \nu_{ei}},\ \kappa_0 = \frac{n_e T_e}{m_e \nu_{ei}}.$$

Equations (2.8) are polynomial approximations to the integrals over the assumed drifting Maxwellian electron distribution that give the various transport coefficients. The dimensionless parameters used are functions only of the plasma ionization state Z, and are shown in the following table for Z=1:

α_0	1.837
α_1	6.416
β_0	3.053
β_1	1.5
γ_0	4.664
γ_1	11.92
δ_0	3.77
δ_1	14.79

The variation of $\kappa_\perp$, $\alpha_\perp$, and $\beta_\wedge$ with the Hall parameter is plotted in Figure 2.1.

We have implemented a flux-conserving numerical scheme to solve Eq. (2.6) for a specified plasma drift velocity, v_e, and successfully tested it for a hydrogen plasma with temperature and density parameters similar to those of the HyperV plasma jet experiments.

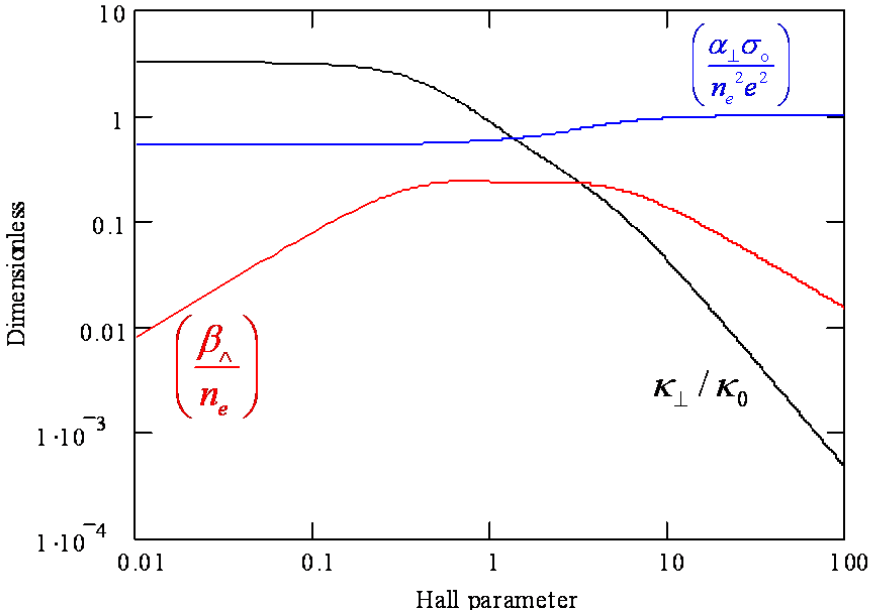

Figure 2.1. Variation of transport coefficients with Hall parameter for 1-D electron temperature equation (Z=1 assumed).

3. Radiative Transport Algorithm Development for LSP

Prism has developed multi-dimensional, multi-frequency radiation transport modeling for use in the LSP code. These algorithms utilize flux-limited radiation diffusion, and they have been developed to support 1-D and 2-D LSP simulations in Cartesian (*x*-*y*), cylindrical (*r*-*z*), and spherical geometries (*r*-θ). These routines utilize Prism's equation-of-state and multi-frequency opacity data tables, and support running in parallel on Linux clusters. This provides LSP with a state-of-the-art capability for performing 2-D simulations with high-quality radiation physics.

Two-dimensional Radiation Diffusion Modeling

Flux-limited diffusion modeling is a commonly-used radiation transport technique in multi-dimensional radiation-hydrodynamics simulation codes due to its relative simplicity and great computational efficiency. Flux-limited diffusion was introduced in astrophysics by Wilson as a method for solving the radiation transport equation [10]. Subsequently, Levermore & Pomraning [11] generalized the theory of flux-limited diffusion as an approximate method for handling transport phenomena which preserves causality in regions where significant spatial variations can occur over distances smaller than a mean free path.

The key ingredient to all such formulations of flux-limited diffusion is the assumption that the specific intensity is a slowly varying function of space and time. This assumption is valid in both the diffusion and streaming limits (at least in one dimension) and is approximately true in the intermediate situations and in multi-dimensions. Given this assumption, analytic relations between the angular moments of various orders may be written. In particular, radiation flux can be expressed in the form of Fick's law of diffusion:

$$\mathbf{F} = -D\nabla E \,, \tag{3.1}$$

where E is radiation energy density, and the diffusion coefficient D can be written as:

$$D = \frac{c\lambda}{\chi} \,. \tag{3.2}$$

The dimensionless function $\lambda=\lambda(E)$ is called the flux limiter, c is the speed of light, and χ is the sum of absorption (k) and scattering (σ) coefficients. A large number of expressions for the flux limiter are possible depending upon different assumptions of the specific intensity angular dependence.

In the diffusion approximation, the radiation transport equation can be written as:

$$\frac{\partial E}{\partial t} - \nabla \cdot D\nabla E = 4\pi kB - ckE \,, \tag{3.3}$$

where B is the Planck function.

When solving this equation numerically, the major challenge is the spatial finite difference approximation in the diffusion term. When written for a particular coordinate system, the diffusion operator assumes the following forms:

$$\nabla \cdot D\nabla E = \frac{\partial}{\partial x} D \frac{\partial}{\partial x} E + \frac{\partial}{\partial y} D \frac{\partial}{\partial y} E \qquad \text{(Cartesian } x\text{-}y \text{ geometry)} \tag{3.4}$$

$$\nabla \cdot D\nabla E = \frac{1}{r}\frac{\partial}{\partial r} rD \frac{\partial}{\partial r} E + \frac{\partial}{\partial z} D \frac{\partial}{\partial z} E \qquad \text{(cylindrical } r\text{-}z \text{ geometry)} \tag{3.5}$$

$$\nabla \cdot D\nabla E = \frac{1}{r^2}\frac{\partial}{\partial r} r^2 D \frac{\partial}{\partial r} E + \frac{1}{r^2 \sin(\theta)}\frac{\partial}{\partial \theta} \sin(\theta) D \frac{\partial}{\partial \theta} E \quad \text{(spherical } r\text{-}\theta \text{ geometry)} \tag{3.6}$$

There are several numerical recipes for discretizing and solving diffusion equations. One of the schemes, developed by Kershaw [12], is used in several multi-dimensional radiation-hydrodynamics codes [13]. Details of the numerical implementation of radiation diffusion algorithms are also described in Refs. [14-16]. We have utilized the formalism of Kershaw to produce an accurate, robust and efficient radiation diffusion package. Our implementation follows a methodology from a more recent implementation of the Kershaw approach for the 2-D radiation-hydrodynamics code DRACO [13].

To model radiation transport, thermal or electron conduction, we need to develop a finite difference equivalent of the diffusion equation:

$$\frac{\partial f}{\partial t} = \nabla \cdot D\nabla f \ . \tag{3.7}$$

The diffusion coefficient D is a given positive function of space and time, and f is the energy density, also positive. The characteristic relaxation time for most laboratory plasmas is much shorter than the numerical time steps. Thus, to ensure numerical stability, we write this equation in a fully implicit form:

$$\frac{f^{n+1} - f^n}{\Delta t} = \nabla \cdot D\nabla f^{n+1} . \tag{3.8}$$

The fully implicit scheme also gives a correct steady-state solution at large Δt: $\nabla \cdot D\nabla f^{n+1} = 0$.

The next important step is to difference the diffusion operator $\nabla \cdot D\nabla f$. For cylindrical geometry (r-z), the mesh consists of a set of points ($R_{K,L}$, $Z_{K,L}$), where the index K ranges from *1* to K_{max} and L from *1* to L_{max}. Each quadrilateral zone is labeled by the largest (K,L) pair of its corners. Figure 3.1 illustrates the indexing technique. Equation (3.8) can be written as:

$$\frac{f_{K,L}^{n+1} - f_{K,L}^{n}}{\Delta t} = \sum_{K',L'} A_{(K,L),(K',l')} f_{K',L'}^{n+1}, \tag{3.9}$$

or in matrix form

$$f^{n} = \left(I - (\Delta t)A\right) f^{n+1}. \tag{3.10}$$

Matrix *A* must be non-positive definite for the algorithm to be numerically stable. It also has to be constructed in such a way that the energy density remains positive. Furthermore, we require *A* to be symmetrical and use a local nine-point stencil so that the linear system can be efficiently solved. A detailed discussion of these properties can be found in Reference [12].

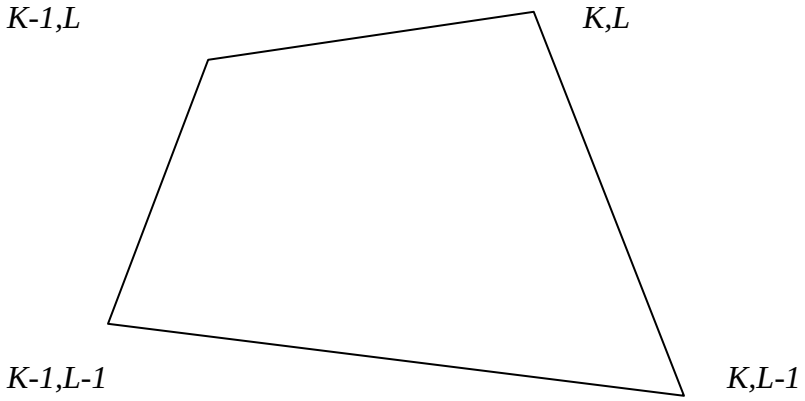

Figure 3.1. Indexing for quadrilateral zone (*K,L*).

It is convenient to specify the coordinates *R* and *Z* as functions of continuous variables *K* and *L*. Then we can define the following quantities:

$$j = \begin{vmatrix} \frac{\partial R}{\partial K} & \frac{\partial R}{\partial L} \\ \frac{\partial Z}{\partial K} & \frac{\partial Z}{\partial L} \end{vmatrix}, \ \mathbf{R_K} = \begin{pmatrix} \frac{\partial R}{\partial K} \\ \frac{\partial Z}{\partial K} \end{pmatrix}, \text{ and } \mathbf{R_L} = \begin{pmatrix} \frac{\partial R}{\partial L} \\ \frac{\partial Z}{\partial L} \end{pmatrix}. \tag{3.11}$$

$\mathbf{R_K}$ and $\mathbf{R_L}$ can be differenced as:

$$\left(\mathbf{R_K}\right)_{K,L} = \left(\mathbf{R}_{K,L} + \mathbf{R}_{K,L-1} - \mathbf{R}_{K-1,L} - \mathbf{R}_{K-1,L-1}\right)/2, \tag{3.12a}$$

$$\left(\mathbf{R_L}\right)_{K,L} = \left(\mathbf{R}_{K,L} + \mathbf{R}_{K-1,L} - \mathbf{R}_{K,L-1} - \mathbf{R}_{K-1,L-1}\right)/2, \tag{3.12b}$$

and

$$C_{K,L} = \left(\mathbf{R_K}\right)_{K,L} \cdot \left(\mathbf{R_L}\right)_{K,L}, \tag{3.12c}$$

We introduce the cell volume as:

$$V_{K,L} = (R \cdot j)_{K,L} = VOLUME / 2\pi\,, \tag{3.13}$$

and quantities $\Sigma_{K,L}$ and $\Lambda_{K,L}$ ($(DR/j)^{1/2}$) averaged over neighboring cells:

$$\Sigma^2_{K,L} = \frac{R_{K,L} + R_{K,L-1}}{j_{K,L}/D_{K,L} + j_{K+1,L}/D_{K+1,L}}, \tag{3.14}$$

$$\Lambda^2_{K,L} = \frac{R_{K,L} + R_{K,L+1}}{j_{K,L}/D_{K,L} + j_{K,L+1}/D_{K,L+1}} \tag{3.15}$$

Then, the coefficients for matrix *A* can be obtained according to the following recipe:

$$V_{K,L}A_{(K,L),(K,L)} = -\sigma_{(K,L)} - \sigma_{(K-1,L)} - \lambda_{(K,L)} - \lambda_{(K,L-1)} + , \\ \left(\rho^1_{(K,L)} + \rho^2_{(K,L)} - \rho^3_{(K,L)} - \rho^4_{(K,L)}\right)/2\,, \tag{3.16a}$$

$$V_{K,L}A_{(K,L),(K+1,L)} = \sigma_{(K,L)} - \left(\rho^1_{(K,L)} + \rho^2_{(K+1,L)} - \rho^3_{(K+1,L)} - \rho^4_{(K,L)}\right)/4\,, \tag{3.16b}$$

$$V_{K,L}A_{(K,L),(K,L+1)} = \lambda_{(K,L)} - \left(\rho^1_{(K,L)} + \rho^2_{(K,L+1)} - \rho^3_{(K,L)} - \rho^4_{(K,L+1)}\right)/4\,, \tag{3.16c}$$

$$V_{K,L}A_{(K,L),(K+1,L+1)} = -\left(\rho^3_{(K+1,L)} + \rho^4_{(K,L+1)}\right)/4\,, \tag{3.16d}$$

$$V_{K,L}A_{(K,L),(K-1,L+1)} = \left(\rho^1_{(K-1,L)} + \rho^2_{(K,L+1)}\right)/4\,, \tag{3.16e}$$

where

$$\sigma_{(K,L)} = \left(\Sigma_{(K,L)}\right)^2 \left(\left(\mathbf{R_L}\right)^2_{K,L} + \left(\mathbf{R_L}\right)^2_{K+1,L}\right)/2\,, \tag{3.17a}$$

$$\lambda_{(K,L)} = \left(\Lambda_{(K,L)}\right)^2 \left(\left(\mathbf{R_K}\right)^2_{K,L} + \left(\mathbf{R_K}\right)^2_{K,L+1}\right)/2\,, \tag{3.17b}$$

$$\rho^1_{(K,L)} = \Sigma_{(K,L)}\Lambda_{(K,L)}C_{K,L}\,, \tag{3.17c}$$

$$\rho^2_{(K,L)} = \Sigma_{(K-1,L)}\Lambda_{(K,L-1)}C_{K,L}\,, \tag{3.17d}$$

$$\rho^3_{(K,L)} = \Sigma_{(K-1,L)}\Lambda_{(K,L)}C_{K,L}\,, \tag{3.17e}$$

$$\rho^4_{(K,L)} = \Sigma_{(K,L)}\Lambda_{(K,L-1)}C_{K,L}\ . \tag{3.17f}$$

Since matrix *VA* is symmetric, $V_{K',L'}A_{(K',L'),(K,L)} = V_{K,L}A_{(K,L),(K',L')}$, and the rest of the coefficients are zero. The resulting matrix is a sparse symmetric nine-diagonal system that can be readily solved to obtain the radiation energy density at the *n+1* time step. Note, that if the mesh is orthogonal, $\rho^1 = \rho^2 = \rho^3 = \rho^4 \equiv 0$ and the system reduces to the standard five point approximation.

Flux Limiter

The diffusion coefficient *D* in Eq. (3.7) is commonly written as $1/3\sigma$ in the classical (unlimited) diffusion approximation, where σ is the local opacity. In a finite difference approximation, the diffusion operator is embedded in the quantities $\Sigma_{K,L}$ and $\Lambda_{K,L}$ (see Eqs. (3.14) and (3.15)) averaged over neighboring cells. In the diffusive limit, the diffusion approximation is first-order accurate. However, in the optically thin limit (small σ), the approximation breaks down allowing for infinite propagation velocities. To correct the problem, flux limiters are commonly introduced. One well-known form, which retains first-order accuracy in the optically thick limit, can be written as:

$$D = \left[(3\sigma)^n + \left(\delta \frac{|\nabla f|}{f} \right)^n \right]^{-1/n}, \tag{3.18}$$

where *f* is the radiation energy density, and δ is a numerical multiplicative factor (flux limiter). When δ is equal to zero, the unlimited case is restored.

Boundary Conditions

Generally, there are two important types of boundary conditions in radiation transport problems:

$$d\mathbf{S} \cdot \nabla f = 0 \text{ (reflective)}, \tag{3.19}$$

and

$$f = f_B \text{ (transparent)}, \tag{3.20}$$

where f_B is a known external radiation energy density. To treat potentially irregular-shaped zone boundaries on a logically rectangular grid, physical zones are completely surrounded by ghost zones. To properly incorporate boundary conditions into the numerical scheme, quantities $\Sigma_{K,L}$ and $\Lambda_{K,L}$ need to be modified in the ghost zones. The following rules are used to determine the quantities [12]:

- If both (K,L) and (K+1,L) are physical zones: $\Sigma_{K,L}(\mathbf{R}_L)_{K,L}$ and $\Sigma_{K,L}(\mathbf{R}_L)_{K+1,L}$ remain unmodified.
- If both (K,L) and (K+1,L) are ghost zones: $\Sigma_{K,L} = 0$

- If (K,L) is a physical zone, and (K+1,L) is a ghost zone, and the face separating the two zones is reflective: $\Sigma_{K,L} = 0$ and $(\mathbf{R}_L)_{K,L}$ is replaced with $\hat{n}(\hat{n}(\mathbf{R}_L)_{K,L})$, where $\hat{n}$ is the unit normal to the ghost surface.
- If (K,L) is a ghost zone, and (K+1,L) is a physical zone, and the face separating the two zones is reflective $\Sigma_{K,L} = 0$ and $(\mathbf{R}_L)_{K+1,L}$ is replaced with $\hat{n}(\hat{n}(\mathbf{R}_L)_{K+1,L})$.
- If (K,L) is a physical zone, and (K+1,L) is a ghost zone, and the face separating the two zones is transparent: $\Sigma_{K,L}(\mathbf{R}_L)_{K,L}$ and $\Sigma_{K,L}(\mathbf{R}_L)_{K+1,L}$ remain the same except that $\Sigma_{K,L}$ is now averaged between zone (K,L) and the vacuum, and $(\mathbf{R}_L)_{K,L}$ is replaced with $\hat{n}(\hat{n}(\mathbf{R}_L)_{K,L})$.
- If (K,L) is a ghost zone, and (K+1,L) is a physical zone, and the face separating the two zones is transparent: $\Sigma_{K,L}(\mathbf{R}_L)_{K,L}$ and $\Sigma_{K,L}(\mathbf{R}_L)_{K+1,L}$ remain the same except that $\Sigma_{K,L}$ is now averaged between zone (K+1,L) and the vacuum and $(\mathbf{R}_L)_{K+1,L}$ is replaced with $\hat{n}(\hat{n}(\mathbf{R}_L)_{K+1,L})$.

A completely analogous set of rules exists for $\Lambda_{K,L}$.

4. Implementation of Radiation Physics Modeling in LSP

Radiation Heating and Cooling

In LSP, electrons and ions can be treated either as kinetic particles or fluid particles. We have implemented a radiation cooling model that can be applied in either case. The rate of change of the electron energy density ε_e due to radiation is given by:

$$\left.\frac{\partial \varepsilon_e}{\partial t}\right|_{rad} = -\int 4\pi \eta_\nu^t d\nu + \int c\kappa_\nu E_\nu d\nu \tag{4.1}$$

where η_ν^t is the "true" or thermal emissivity, κ_ν is the absorption coefficient, and E_ν is the radiation energy density, all evaluated at radiation frequency ν. In LTE, the "source function", which is the ratio of the emissivity to the opacity, is given by the Planck function evaluated at the local electron temperature T_e [17]:

$$B_\nu(T_e) = \frac{2h\nu^3}{c^2}\frac{1}{e^{h\nu/kT_e}-1} \tag{4.2}$$

and the thermal emissivity in Eq. (4.1) is then obtained from the detailed-balance relation:

$$\eta_\nu^t = \kappa_\nu B_\nu(T_e) \tag{4.3}$$

The term for electron radiation cooling implemented in LSP is:

$$\left.\frac{\partial \varepsilon_e}{\partial t}\right|_{rad} = -\int 4\pi \kappa_\nu B_\nu(T_e) d\nu \tag{4.4}$$

The right-hand side is a function only of local density and electron temperature, so that the integral can be tabulated in a 2-D lookup table. One can define a mean emission opacity, κ_P, through

$$\int \kappa_\nu B_\nu(T_e) d\nu \equiv \kappa_P B(T_e), \text{ wh re } B(T_e) \equiv \int B_\nu(T_e) d\nu = \frac{\sigma_R T_e^4}{\pi} \tag{4.5}$$

and $\sigma_R \equiv 2\pi^5 k^4 / 15c^2 h^3$ is the Stefan-Boltzmann constant. Equation (4.4) is then written equivalently as:

$$\left.\frac{\partial \varepsilon_e}{\partial t}\right|_{rad} = -4\kappa_P \sigma_R T_e^4 \tag{4.6}$$

In the LSP implementation, κ_P is obtained for local values of the ion density and electron temperature by calling the lookup functions. These functions access the PROPACEOS data tables provided by Prism.

In the algorithm, the updated value of ε_e must be converted to a new value of the local electron temperature T_e. In general, the energy radiated by the electrons comes from a combination of free-free, free-bound, and bound-bound transitions. The

PROPACEOS data files contain a table of the electron specific internal energy as a function of the ion density and electron temperature. The electron temperature is therefore obtained by doing a reverse lookup using ε_e from Eq. (4.6). If the electron temperature is sufficiently high so that the number of free electrons does not change due to the radiation and the change in electron potential energy can be neglected, then the change in ε_e in Eq. (4.6) is due entirely to a change in the kinetic energy of the free electrons. We can then write:

$$\frac{3}{2} n_e \left. \frac{\partial T_e}{\partial t} \right|_{rad} = -4\kappa_P \sigma_R T_e^4 \tag{4.7}$$

Having updated T_e, we can update the electron kinetic energy using the LTE assumption of a local Maxwellian distribution, for which the average electron kinetic energy is $3kT_e/2$. For a "kinetic" treatment of the electrons, where the electrons have only position and momentum variables, we update each component of the momentum on a cell-by-cell basis using the equation:

$$p_i' = \langle p \rangle + \left(p_i - \langle p \rangle \right) \sqrt{\frac{T_e'}{T_e}}, \tag{4.8}$$

where p_i is the momentum of the i^{th} electron in the cell, and $\langle p \rangle$ is the average momentum of the electrons in the cell. This procedure changes the *rms* electron momentum in the cell to a value consistent with the new local temperature T_e'. For a "fluid" treatment of the electrons, the right-hand side of Eq. (4.7) is added to the existing electron energy equation to obtain:

$$\frac{3}{2} n_e \frac{dT_e}{dt} = -n_e T_e \nabla . \mathbf{v}_e + \nabla . \kappa_e \nabla T_e + \frac{3 m_e n_e}{m_i \tau_{ei}} \left(T_i - T_e \right) + m_e \nu_{ei} \left(\mathbf{v}_e - \mathbf{v}_i \right)^2 - 4\kappa_P \sigma_R T_e^4 \tag{4.9}$$

where κ_e is the electron thermal conductivity, τ_{ei} is the electron-ion energy exchange timescale, T_i is the local ion temperature, $\mathbf{v}_e$ and $\mathbf{v}_i$ are the electron and ion drift velocities, respectively, and ν_{ei} is the electron-ion momentum-transfer frequency.

5. LSP Test Simulations with Radiation Transport Modeling

Benchmark Simulations: Comparison with Analytic Solutions

A variety of analytical solutions exist for one-dimensional diffusion problems. To simulate a pseudo-one-dimensional system within a two-dimensional diffusion framework, we apply reflective conditions on the top and bottom boundaries thus letting radiation propagate in the horizontal direction. The first problem tests numerical differencing inside the medium. We assume constant opacities and neglect radiation emission/absorption by the plasma so that only transport algorithms are tested. We use a 51 x 51 orthogonal grid, and the flux limiter is turned off. We apply a delta function source in a X = 1 cm wide slab of otherwise cold plasma at time zero ($f(x=X/2,t=0) = Q\,\delta(x=X/2)$). The analytic solution to this problem has the form:

$$f(x,t) = \frac{Q}{\sqrt{4\pi Dt}} e^{-\frac{\left(x-X/2\right)^2}{4Dt}}, \qquad (5.1)$$

where D is the diffusion coefficient. Figure 5.1 compares numerical and analytical solutions at different times. The numerical simulations are seen to be in excellent agreement with the analytic solutions.

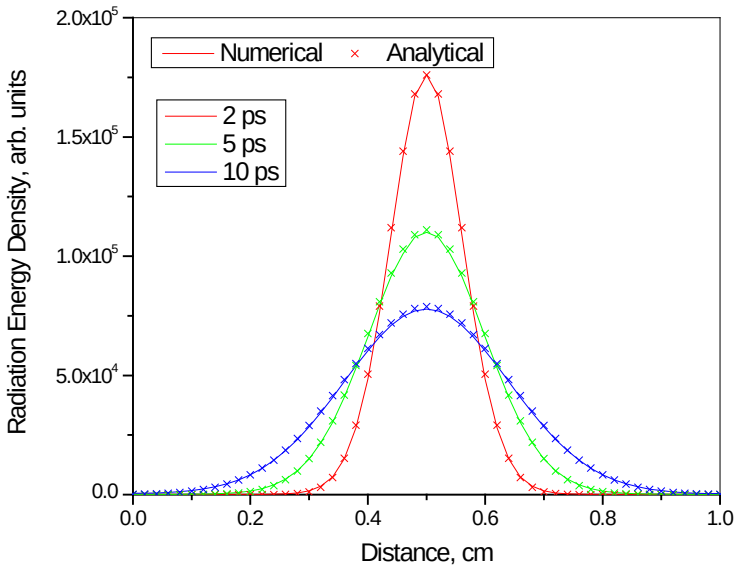

Figure 5.1. Comparison between analytical and numerical solutions with a delta function source.

To test the numerical differencing and boundary conditions, we use the same assumptions as in the previous case, except we apply radiation boundary conditions on the left and right sides. The radiation energy density in the steady state should vary linearly with position between the values at the boundaries, as is shown in Figure 5.2.

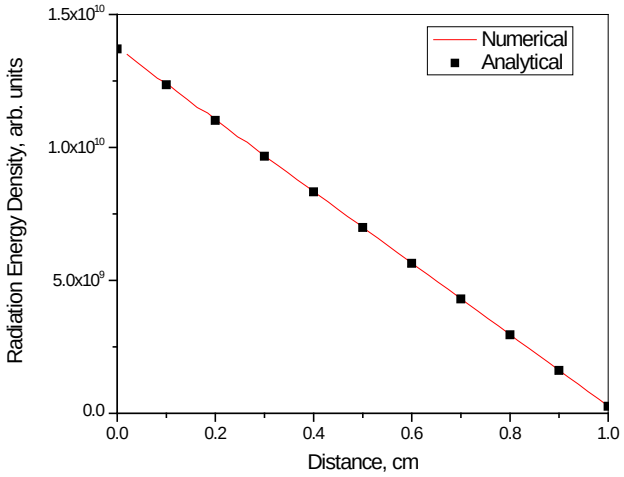

Figure 5.2. Comparison between analytical and numerical solutions with radiation boundary conditions (no emission/absorption).

The third test is completely analogous to the second, except the plasma emission and absorption terms are included. The radiation temperature in this case can be expressed as follows:

$$T_r(x) = T_0 \left(\frac{\frac{1}{2}\left(\frac{1}{2}+D\lambda\right)e^{\lambda(X-x)} - \left(\frac{1}{2}-D\lambda\right)e^{-\lambda(X-x)}}{\left(\frac{1}{2}+D\lambda\right)^2 e^{\lambda X} - \left(\frac{1}{2}-D\lambda\right)^2 e^{-\lambda X}} \right)^{1/4}, \qquad (5.2)$$

where T_0 is the radiation temperature at the boundary, λ is the inverse diffusion length:

$$\lambda = \sqrt{\frac{\sigma}{D}} = \sqrt{3}\sigma \ , \qquad (5.3)$$

and σ is the opacity. Figure 5.3 shows that the agreement between the analytical and numerical solutions is very good.

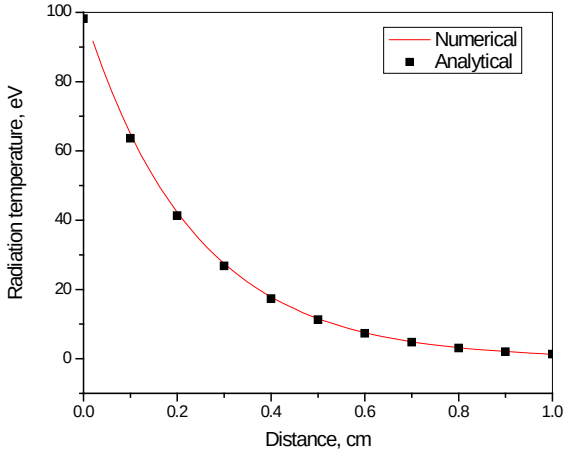

Figure 5.3. Comparison between analytical and numerical solutions with radiation boundary conditions (includes emission/absorption).

Similar benchmark simulations and tests were run for other geometries, with results showing good agreement with analytic solutions. Tests were also performed with distorted grids to test the accuracy and stability of solutions. The benchmark simulations show that the numerical radiation transport algorithms developed for use in LSP are accurate.

Multi-Frequency Test Cases

Several benchmarks have been performed to verify the multi-group diffusion implementation and surface fluxes. Details of the spectral flux not only provide important information for the diagnostics, but are also needed for the overall energy balance.

In the optically thin limit, the emerging spectral flux depends primarily on the details of the frequency-dependent Planck opacity tables. In the optically thick limit, the flux emergent from an isothermal plasma should recover the Planck function (blackbody spectrum) which is characterized only by the plasma temperature, and is independent of the material opacity.

LSP calculations have been performed with 500 group CH_2 opacity tables. Calculations for several values of the plasma size, temperature, and density have been performed (see Figures 5.4 – 5.7). In the optically thin case, the emergent flux reflects the intrinsic spectral line structure of emitted radiation. For optically thick plasmas, the calculated fluxes are well-approximated by the Planck function at the specified temperature regardless of the length of the simulation (reflecting the near equilibrium of radiation with emitting plasma), and the total frequency-integrated flux is proportional to the fourth power of the temperature (Stefan–Boltzmann law). These tests were carried out independently for both Cartesian directions, and also for cylindrical coordinates.

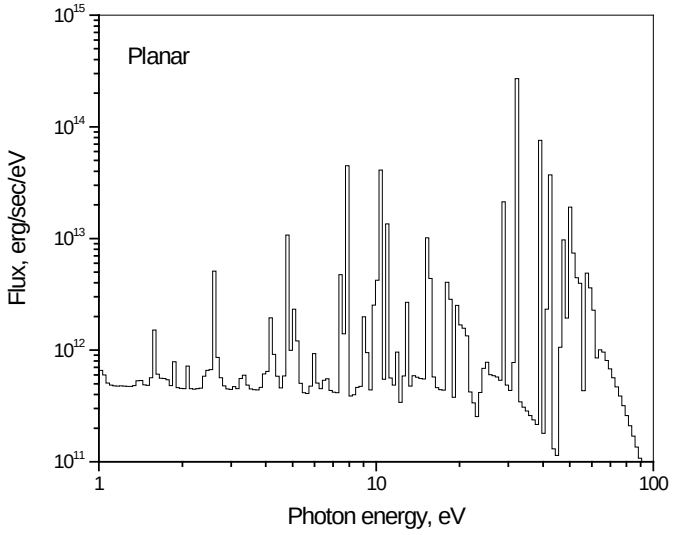

Figure 5.4. Emergent flux for multi-frequency benchmark case for Cartesian coordinates, optically thin plasma.

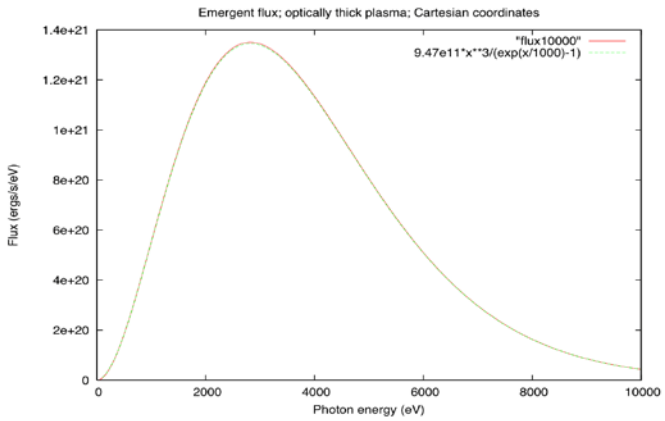

Figure 5.5. Emergent flux for multi-frequency benchmark case for Cartesian coordinates, optically thick plasma.

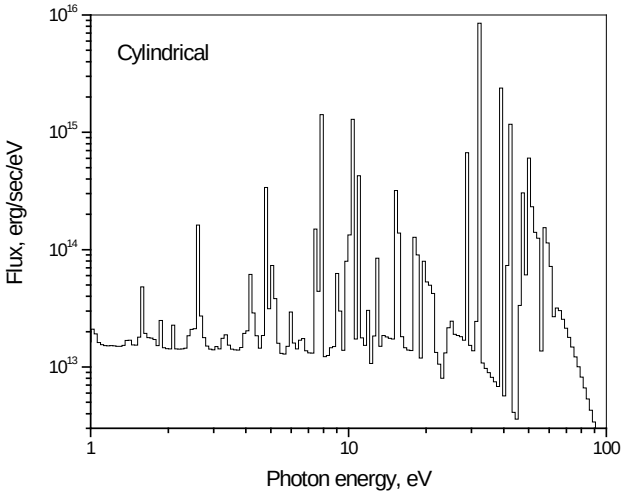

Figure 5.6. Emergent flux for multi-frequency benchmark case for cylindrical coordinates, optically thin plasma.

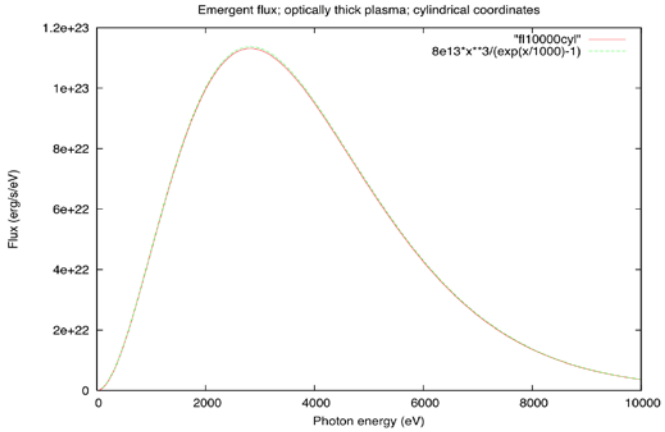

Figure 5.7. Emergent flux for multi-frequency benchmark case for cylindrical coordinates, optically thick plasma.

Comparison of LSP Multi-Frequency Radiation Calculations with Numerical Solutions

Above, we have described an extensive set of benchmark calculations that verify the implementation of a multi-group two-dimensional radiation diffusion model in LSP. We also performed a composite benchmark calculation in order to test radiation-plasma coupling and the equation-of-state implementation. To this end, a LSP calculation was performed with the radiation heating and cooling terms computed and appropriately applied to the plasma energy equations. The results have been compared against a well-benchmarked 1-D radiation-hydrodynamics code *HELIOS* [3].

In the calculation, a plane-parallel slab of CH_2 plasma is allowed to radiate into vacuum and cool. The initial conditions are chosen such that the plasma is optically thin (mass density of 10^{-4} g/cm^3 and size of 1 micron). These conditions result in volumetric cooling of the plasma. The hydrodynamic motion of the plasma is not considered, and the electron-ion interaction is sufficiently large so that equilibration time is much shorter than the characteristic time step. Reflective radiation boundary conditions are applied on two opposite sides of the plasma, while the other two sides are transparent. The above conditions are chosen so that the differences between LSP and *HELIOS* codes which are not relevant to this particular benchmark are minimal. The codes use identical 10 group opacity and EOS data. The initial temperature of the plasma is chosen to be 1000 eV and the calculations runs for two microseconds. Thus, as the plasma cools, it goes through several ionization stages from fully ionized to nearly neutral.

Figure 5.8 shows the time histories of plasma temperature and average ionization, respectively, as computed by *HELIOS*. The corresponding values computed by LSP are shown in Figures 5.9. Good agreement is seen between the two results.

These simulations for this composite benchmark demonstrate that the radiation transport, the radiation-plasma coupling, and the equation-of-state models have been successfully implemented in LSP.

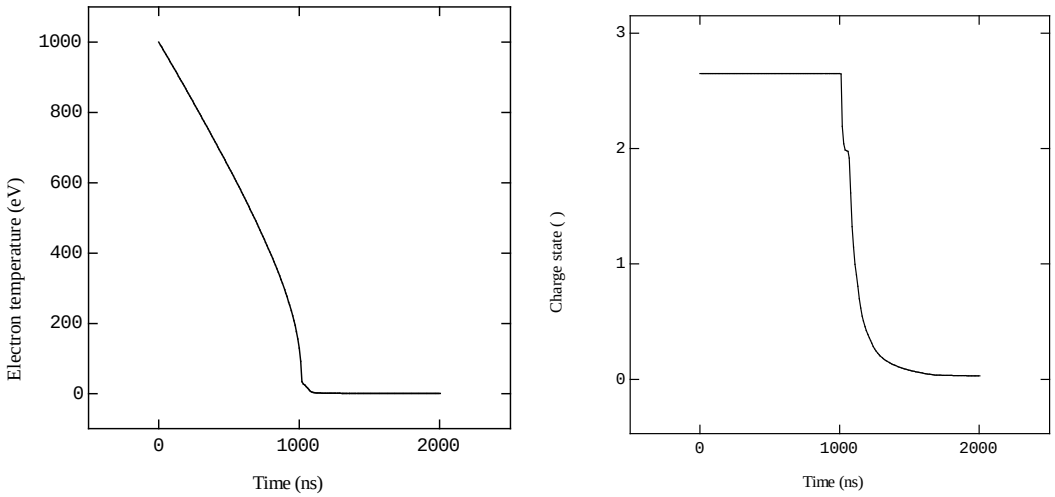

Figure 5.8. Time-dependent electron temperature and plasma charge state from a planar *HELIOS* simulation.

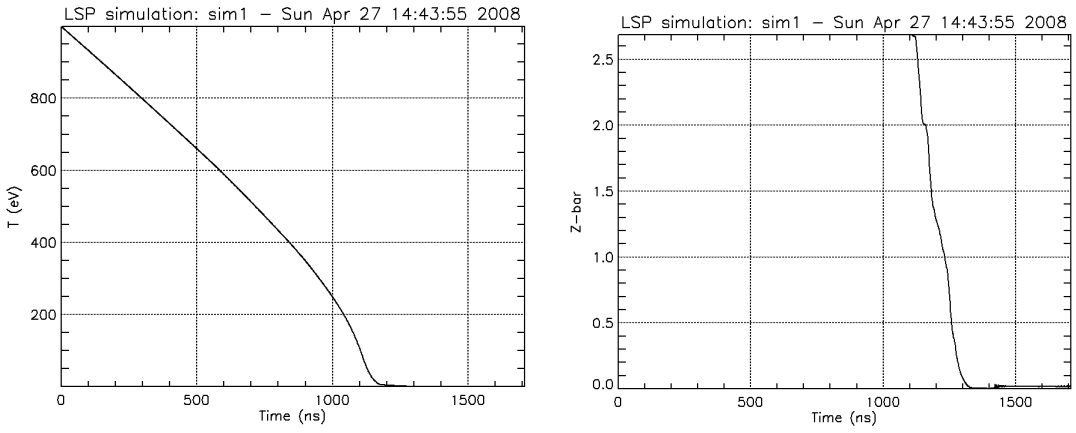

Figure 5.9. Same as Fig. 5.8, but for *LSP*.

6. Upgrades to Atomic Physics Data

Atomic Physics Databases

During this project, Prism generated an updated version of its atomic data library. This library includes atomic energy level and transition data that are required for collisional-radiative spectral analysis codes, ionization dynamics codes, and equation of state and opacity codes. These include collisional excitation and ionization cross sections, photoionization cross sections, oscillator strengths, radiative recombination rate data, and dielectronic recombination rate data. The updated database has several significant improvements, including:

- more detailed energy level modeling and significantly more atomic transitions;
- improved treatment of L-shell dielectronic recombination and electron capture rates;
- utilization of the most recent version of the NIST atomic database [18].

Prism Atomic Data Library is considered to be very detailed and comprehensive. Atomic data is generated using state-of-the-art atomic structure and cross section codes [19]. Calculated data for wavelengths and oscillator strengths are then superseded by data from the NIST atomic data library for those energy levels and transitions that are included in the NIST database. This approach provides atomic data that is considered to be both accurate (because it relies on NIST experimentally-based data when available, and state-of-the-art atomic physics codes otherwise) and comprehensive (as it includes a very large number of energy levels and transitions). For elements of atomic number Z = 1 through 36, the Prism Atomic Data Library contains a total of more than 600,000 atomic energy levels and 40 million atomic transitions. Prism's atomic data have been used extensively to simulate plasma radiation characteristics for a wide variety of applications at major DOE laboratory facilities and for small-scale university laboratory experiments.

Improvements in Equation of State and Opacity Modeling

We have improved the accuracy and stability of EOS modeling, especially in the strongly coupled plasma regime (*i.e.*, at relatively low temperatures and high densities), where a quotidian equation of state (QEOS) model is utilized. The algorithms for merging the QEOS and isolated atom regimes have been updated to provide improved accuracy and robustness. Also, the continuum lowering correction has been improved for mixtures.

We have also performed a number of benchmark calculations using a new version of the EOS and opacity code *PROPACEOS* [3] and the updated Prism Atomic Data Library. The calculations were done for several elements and mixtures for a wide range of temperatures and densities. Special attention was paid to the challenging problem of

accurately modeling L-shell opacities for mid-Z elements (*e.g.*, argon (Z=18) through krypton (Z =36)). This includes elements such as Cu, which may be representative of elements that could be ablated from the electrodes in HyperV experiments. Our EOS results were shown to agree favorably with SESAME data, while our opacity calculations were shown to compare well with TOPS [20] and OPAL [21]. In particular, our opacity data for Fe has been extensively benchmarked against high-resolution transmission data obtained in opacity experiments performed at the *Z* facility [22].

Equation-of-State and Opacity Calculations for Ar and Xe

Opacity and EOS calculations were performed using Prism's *PROPACEOS* code to generate tabular data for Ar and Xe. For each material, the temperature in the EOS/opacity tabular data ranges from 0.01 to 1000 eV, while the ion number density ranges from 10^{16} to 10^{25} ions/cm^3. For the LSP code, multi-group opacity tables were computed for 10 groups, with frequency bins logarithmically spaced over a range of photon energies from 0.1 eV to 100 keV.

The atomic model for Ar included approximately 14,500 atomic energy levels, while that for Xe included approximately 13,500 atomic energy levels for all ionization stages. Due to the complexity of Xe atomic structure, many levels are included as configuration-averaged. The detailed representation of the atomic structure is important for accurate calculation of group opacities, even though the number of photon energy groups may not be sufficient to resolve individual spectral features. Figures 6.1 and 6.2 illustrate, for Ar and Xe, respectively, the detailed contribution to the opacity from multiple atomic transitions by comparing 10 and 1000 group opacities for the same plasma conditions (100 eV temperature and 10^{17} cm^{-3} ion number density).

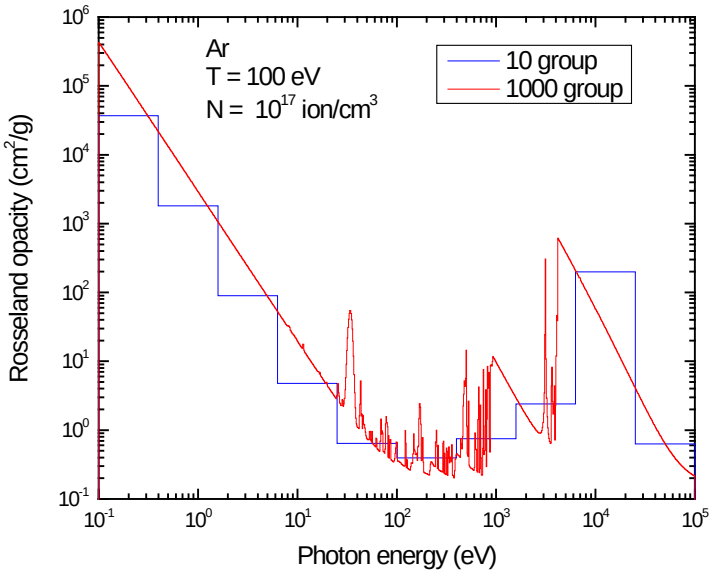

Figure 6.1. Comparison of frequency-dependent Rosseland group opacities computed for Ar for cases with 10 (blue histogram) and 1000 (red histogram) frequency groups. In each case, the temperature is 100 eV and ion density is 10^{17} ions/cm^3.

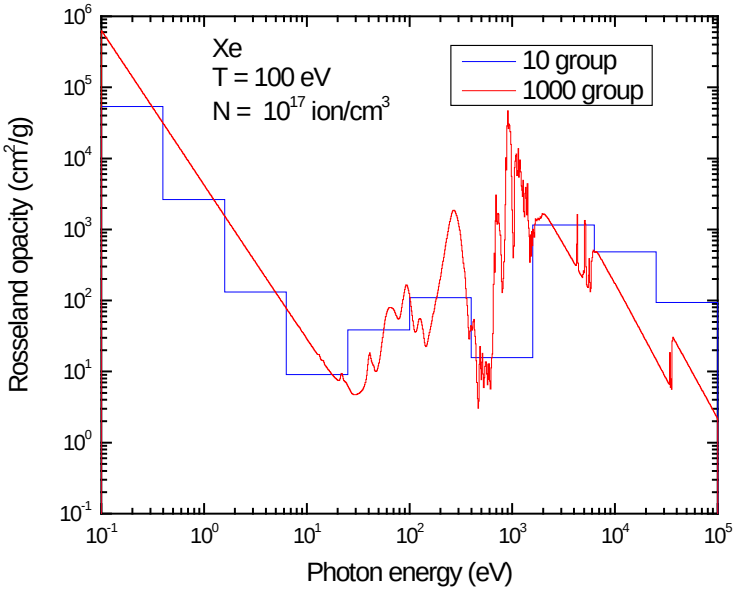

Figure 6.2. Comparison of frequency-dependent Rosseland group opacities computed for Xe for cases with 10 (blue histogram) and 1000 (red histogram) frequency groups. In each case, the temperature is 100 eV and ion density is 10^{17} ions/cm^3.

7. Radiative Cooling Rates for High Velocity Plasma Jets

We have performed a series of simulations of the radiative cooling properties of several materials. Specifically, we examined the temperature sensitivity of radiative cooling rates and characteristic cooling times at densities typical of those in plasma jet experiments.

The radiative cooling rate (R_{emis}) can be written in terms of multi-group opacities as follows:

$$R_{emis} = \frac{8\pi(kT_e)^4}{c^2h^3}\sum_g^{N_F}\left(\sigma_g^{PE}\int_{x_g}^{x_{g+1}}\frac{x^3}{e^x-1}dx\right), \quad x = h\nu/kT_e , \tag{7.1}$$

where g is the photon frequency group index, N_F is the number of frequency groups, h is the Planck constant, k is the Boltzmann constant, T_e is the electron temperature, c is the speed of light, v is the photon frequency, and σ_g^{PE} is the mean Planck emission opacity for frequency group g. In the case of frequency-independent (gray) opacity, the integration can be performed analytically and Eq. (7.1) can be simplified further:

$$R_{emis} = 4\sigma_{SB}T_e^4\sigma^{PE} , \tag{7.2}$$

where σ_{SB} is Stefan-Boltzmann constant, and σ^{PE} is total Planck emission opacity. The cooling rate is typically provided in units of energy per unit mass per unit time.

For a given temperature and density, the characteristic radiative cooling time (T_{RC}) can be computed as a ratio of the total plasma specific energy (E_{total}, units of energy per unit mass) and the cooling rate:

$$T_{RC} = E_{total}/R_{emis} . \tag{7.3}$$

Due to the strong dependence on plasma temperature (T^4), radiative cooling plays a progressively more important role for hotter plasmas, even at short time scales. The plasma opacity and emissivity are also strong non-linear functions of temperature. As the temperature increases, the average charge state increases, and the contribution from different ionization stages to the total opacity changes. Line radiation from different ions may contribute significantly to the plasma opacity and emissivity. Appropriate accounting for this effect can be especially challenging for mid- and high-Z materials. Figure 7.1 illustrates LTE emission opacity and average ionization dependence on temperature for an argon plasma with an ion number density of 1 x 10^{17} cm^{-3}. The average ionization increases with temperature. The relatively flat plateaus correspond to closed-shell configurations (*i.e.*, Ne- and He-like ions, fully ionized). Note that the plasma opacity peaks for temperatures that favor ionization stages in between closed-shell ions. Pronounced peaks for M-shell (orange), L-shell (green), and K-shell (magenta) can be observed. The reason for this behavior is that ions with an incomplete

outer shell contain a very large number of radiatively decaying excited states which contribute to the total opacity and emissivity. This emphasizes the importance of detailed atomic models for computing plasma radiative properties.

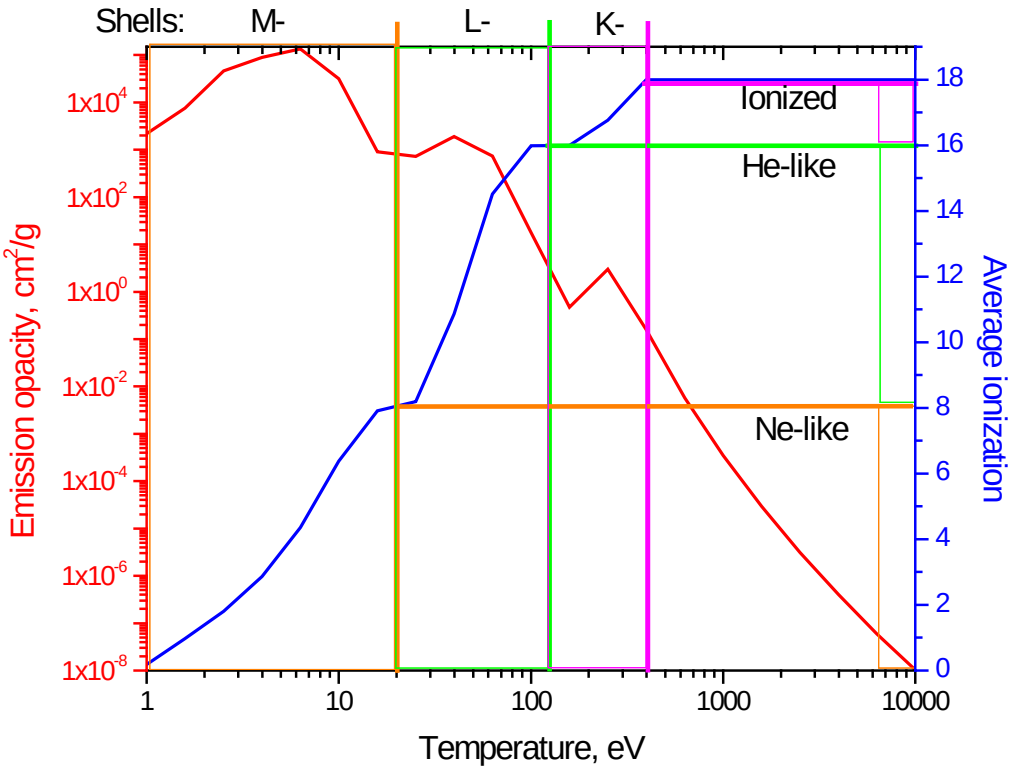

Figure 7.1. Emission opacity (red) and average ionization (blue) for an argon plasma with an ion number density of $1x10^{17}$ cm^{-3}.

Figures 7.2 through 7.7 show the temperature dependence of the radiative cooling rate and the characteristic cooling time for different materials (H, CH, Ar). These calculations were performed using the assumption of local thermodynamic equilibrium (LTE) in computing the atomic level populations and ionization distribution. Results are shown for ion number densities varying from 10^{16} to 10^{18} cm^{-3}. The structure observed at low and moderate temperatures is due to the physical effects described above.

Note that the characteristic cooling times for a pure H plasma are relatively long (τ ~ μsec to tens of msec). By comparison, the characteristic time for the evolution of plasma conditions in plasma jet experiments is ~ μsec. This suggests that the effects of radiative cooling in pure H plasma jets are relatively small. However, the radiative cooling rates for a CH plasma are 1 to 3 orders of magnitude higher, and characteristic radiative cooling times are as short as 100 nsec for a 10^{17} cm^{-3} CH plasma. Thus, radiative cooling effects for CH are likely to become important. For higher-Z materials, radiative cooling becomes even more important, as is seen for the case of Ar.

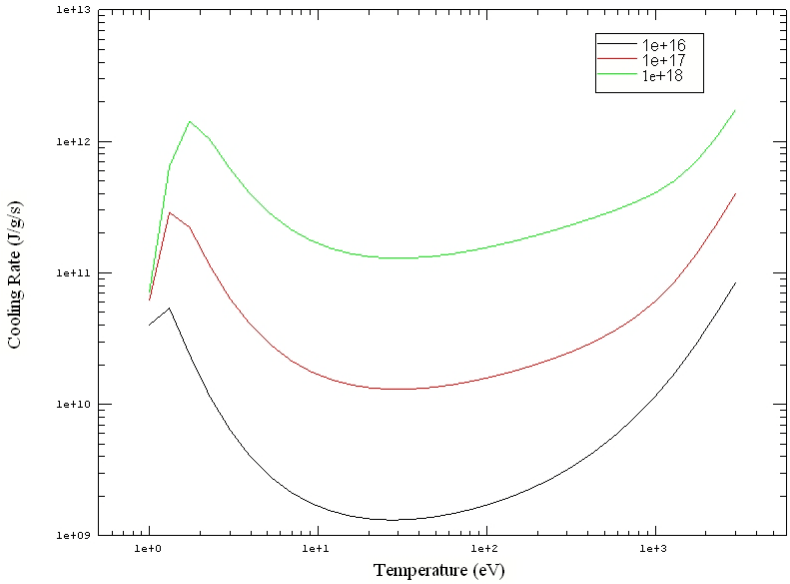

Figure 7.2. Calculated radiative cooling rate vs. temperature for a pure H plasma. Calculations, performed using PROPACEOS, are for ion densities of 10^{16}, 10^{17}, and 10^{18} cm^{-3}.

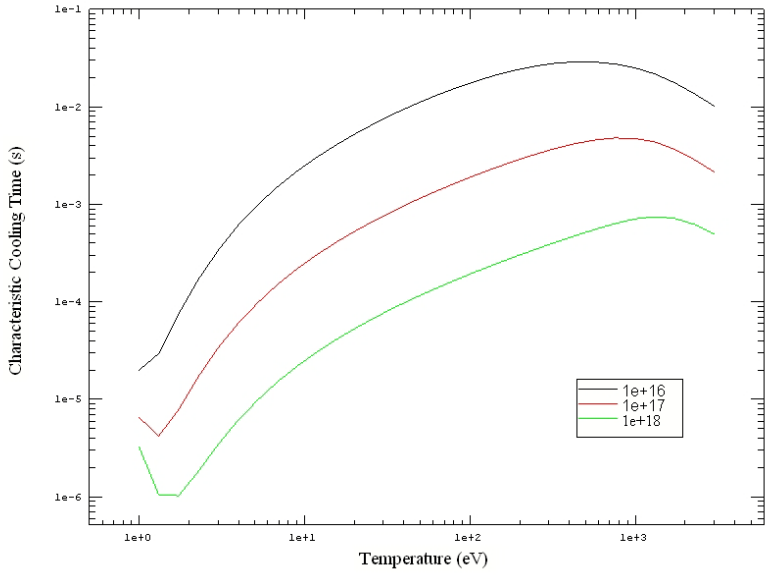

Figure 7.3. Calculated characteristic radiative cooling time vs. temperature for a pure H plasma. Calculations, performed using PROPACEOS, are for ion densities of 10^{16}, 10^{17}, and 10^{18} cm^{-3}.

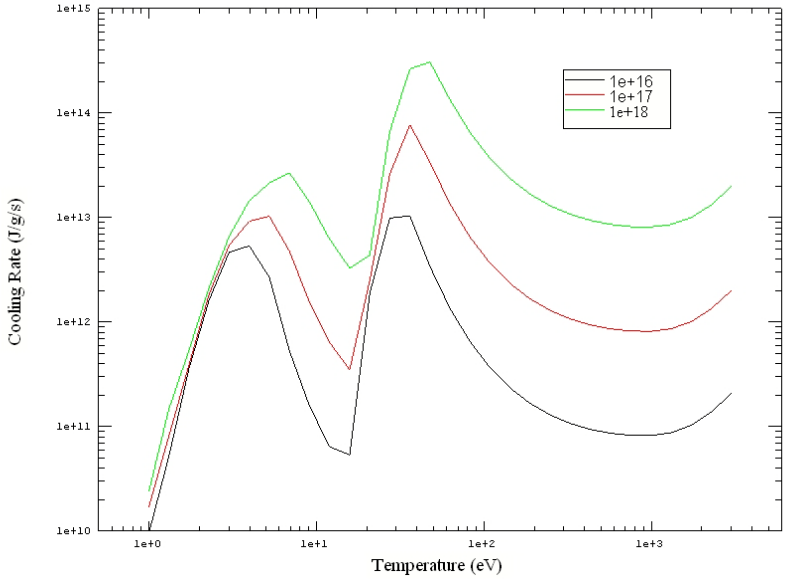

Figure 7.4. Same as Fig. 7.2, but for CH.

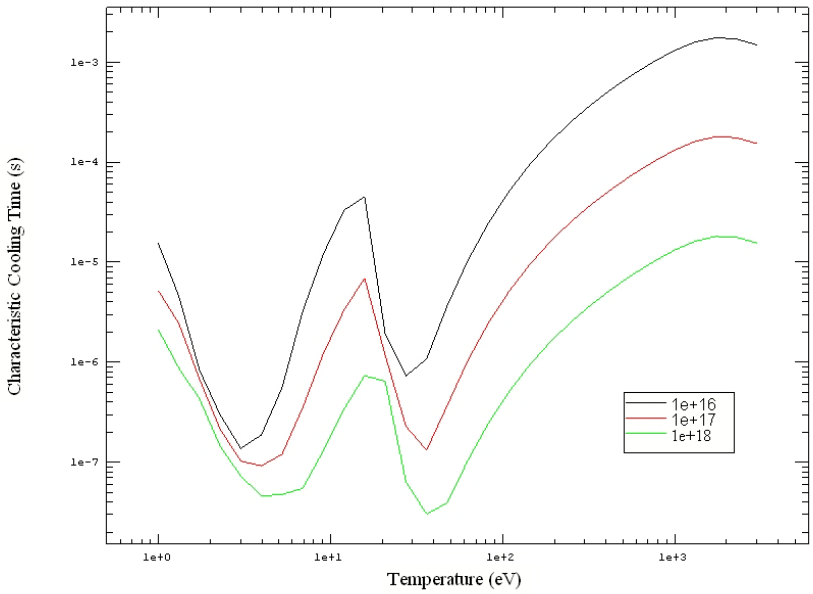

Figure 7.5. Same as Fig. 7.3, but for CH.

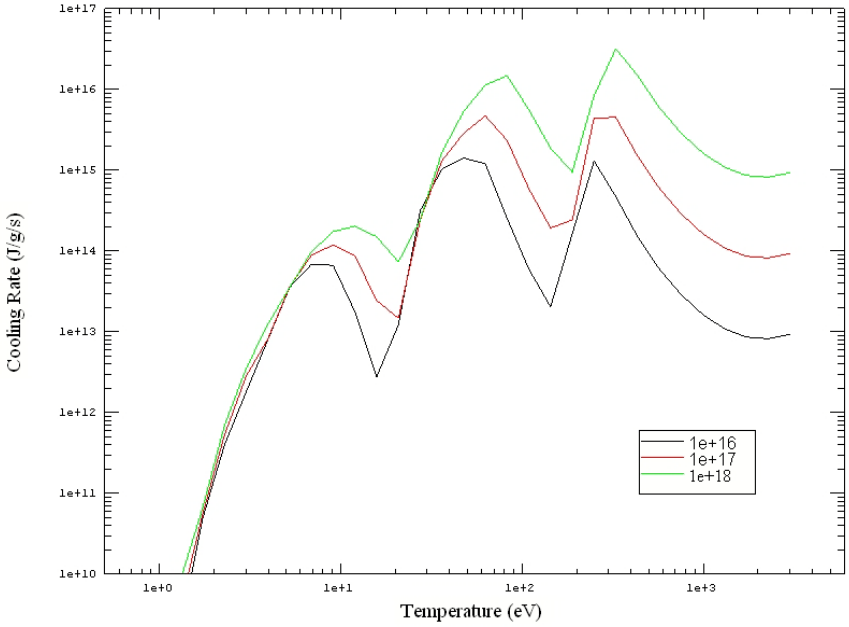

Figure 7.6. Same as Fig. 7.2, but for Ar.

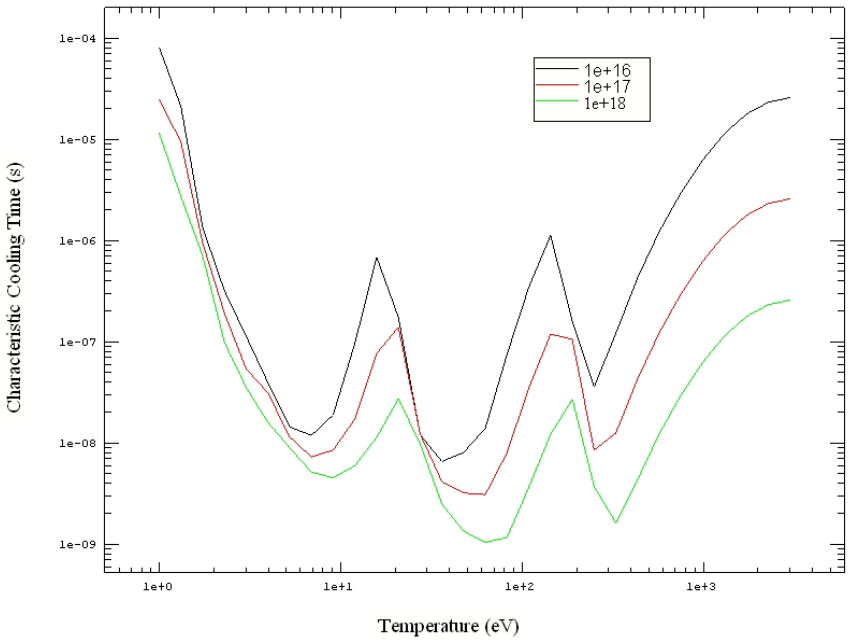

Figure 7.7. Same as Fig. 7.3, but for Ar.

8. Effect of Electrode Contaminants on Plasma Jet Radiative Cooling

In plasma jet experiments, it is possible that a small concentration of material from the electrode can become vaporized and embedded in the plasma jet. To estimate the amount of electrode material required to alter the radiative properties of the plasma, we have performed an initial series of calculations for a H plasma with a variable concentration of Cu (Z = 29) mixed into the plasma. (We note the radiative cooling properties of Cu are similar to that of elements of similar atomic number (*e.g.*, Fe, Co, Ni)).

Three series of PROPACEOS calculations were performed for H-Cu plasma mixtures, with the Cu concentration varying from 10^{-5} to 10^{-1} by number. These calculations were performed under the assumption of LTE. The results for radiative cooling rates and characteristic radiative cooling times, as defined in Section 7, are shown in Figures 8.1 through 8.6. These results can be compared with those discussed in Section 7 (*e.g.*, see Figs. 7.2 and 7.3 for pure H).

While Figure 7.3 shows that the characteristic radiation cooling times for a pure H plasma is $\gtrsim 10^{-6}$ sec, the introduction of small amounts of Cu significantly increases the cooling rate, and shortens the characteristic cooling time. For example, the cooling times for 10% Cu (Figures 8.1 and 8.2) and 0.1% Cu (Figures 8.3 and 8.4) at a plasma temperature ~ 30 eV and density ~ 10^{17} ions/cm^3 are ~ 2 nsec and 60 nsec, respectively. These cooling times are short compared to the characteristic time over which plasma conditions change in plasma jet experiments of interest to this study. Not until Cu concentrations fall to ~ 10^{-5} (see Figures 8.5 and 8.6) do characteristic cooling times stay above 1 μsec. This suggests that the ablation (vaporization) of electrode material in plasma jet experiments may – by increasing radiative energy loss effects – play a critical role in the overall energetics of the plasma evolution if the electrode material concentration exceeds ~ 10^{-4} (0.01%).

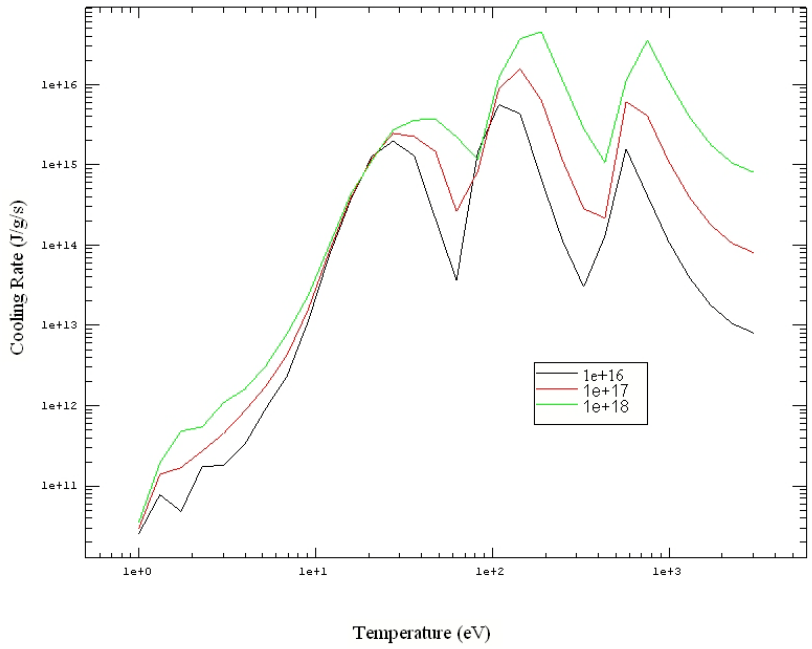

Figure 8.1. Calculated radiative cooling rate vs. temperature for a H-Cu plasma mixture, with 10% Cu by number. Calculations, performed using PROPACEOS, are for ion densities of 10^{16}, 10^{17}, and 10^{18} cm^{-3}.

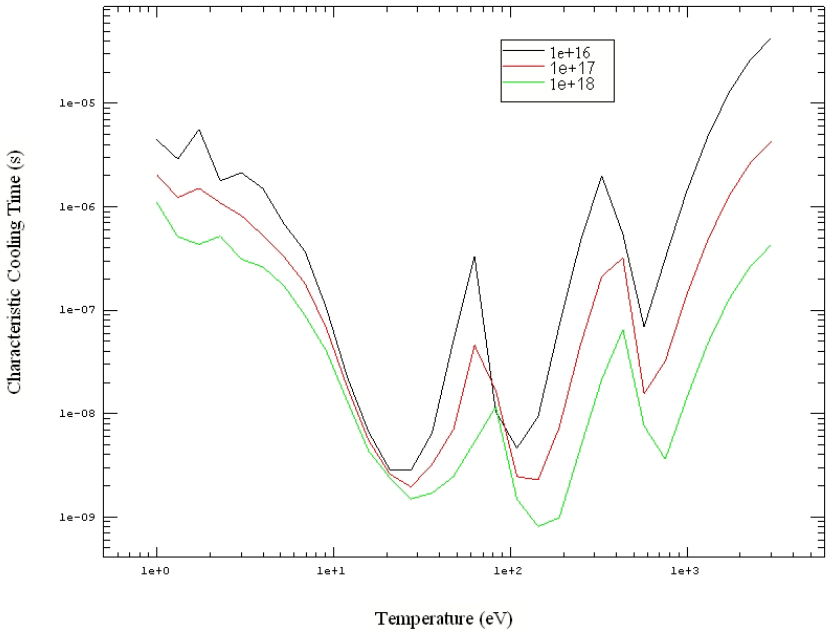

Figure 8.2. Calculated characteristic radiative cooling time vs. temperature for a H-Cu plasma mixture, with 10% Cu by number. Calculations, performed using PROPACEOS, are for ion densities of 10^{16}, 10^{17}, and 10^{18} cm^{-3}.

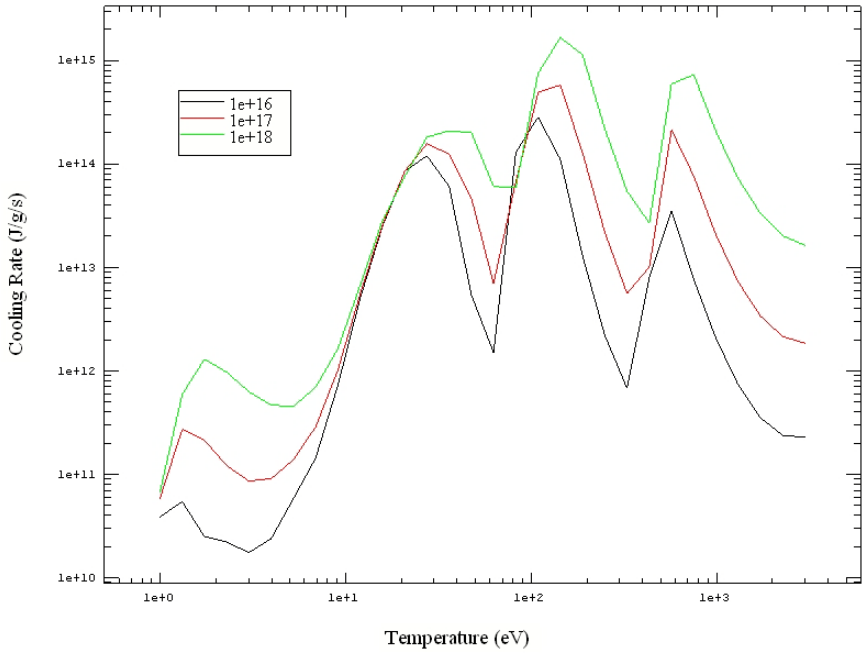

Figure 8.3. Same as Fig. 8.1, but for a H-Cu plasma mixture, with 0.1% Cu by number.

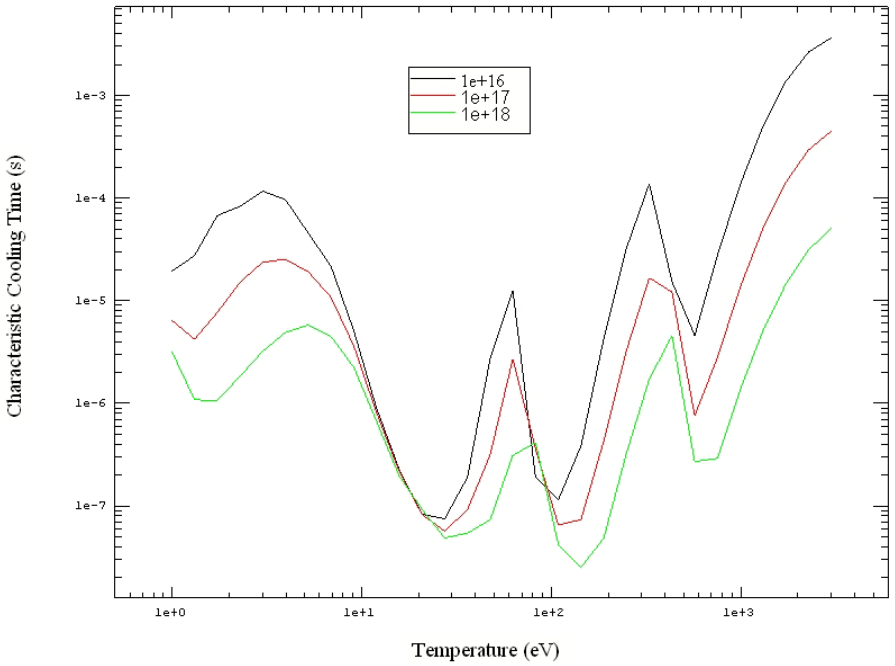

Figure 8.4. Same as Fig. 8.2, but for a H-Cu plasma mixture, with 0.1% Cu by number.

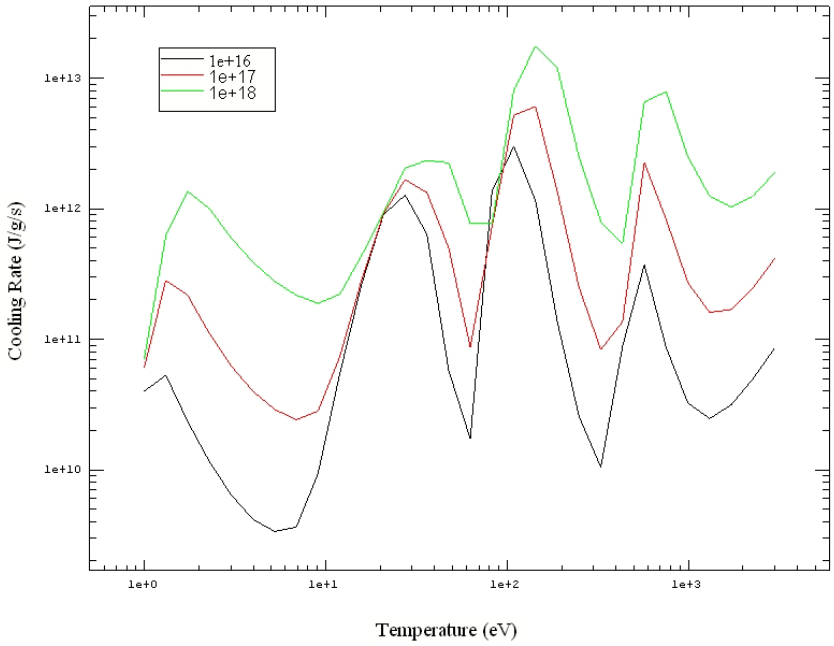

Figure 8.5. Same as Fig. 8.1, but for a H-Cu plasma mixture, with 0.001% Cu by number.

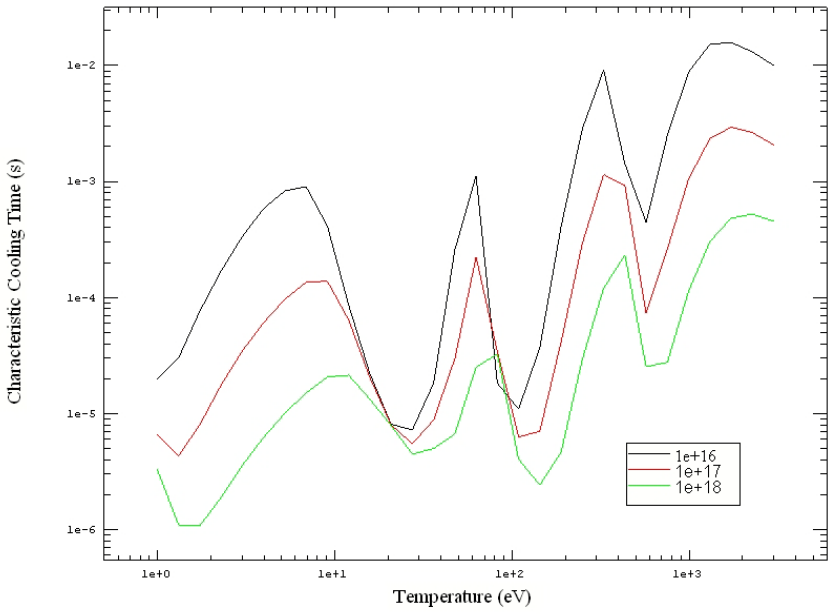

Figure 8.6. Same as Fig. 8.2, but for a H-Cu plasma mixture, with 0.001% Cu by number.

9. SPECT3D Modeling

SPECT3D [4] is a multi-dimensional collisional-radiative imaging and spectral analysis package. One of its major functions is to post-process output from multi-dimensional radiation-hydrodynamics simulations to generate simulated spectra and images that can be directly compared with experimental measurements. By doing this, it provides a means of comparing simulation predictions with experimental observations, and therefore assessing the accuracy and reliability of physics models in the simulation codes. SPECT3D is used at several major DOE laboratories, including Sandia National Laboratories and the Laboratory for Laser Energetics at the University of Rochester, to post-process output from a variety of codes (*e.g.*, DRACO, LASNEX, HYDRA, and ALEGRA).

For LSP, we have updated SPECT3D to be able to post-process output from LSP simulations. This will allow us to generate simulated images and spectra that can be compared with data obtained in HEDP experiments. In addition, we have made significant updates to SPECT3D that will allow us to post-process the output from large-scale 2-D and 3-D hydro/PIC simulations. The updates are discussed below.

SPECT3D-LSP Interface Development

To facilitate post-processing of LSP output using SPECT3D, we have added the capability to LSP to generate output files in a NetCDF [23] format. This has a number of advantages over standard binary or ascii output, including: compactness of data; ability to move data across platforms; and ability to utilize/view data while the simulation is in progress. Additionally, the format is the same regardless of which NetCDF library is used to write it (Fortran 77, Fortran 90, C or C++).

When a plasma simulation is run using SPECT3D, the hydrodynamics data for each cell in the plasma is read from a file in NetCDF format. The data required by SPECT3D are:

- The time (in seconds)
- The node positions (in cm or m)
- An array describing the node indices that make up each cell
- The electron temperature in each cell
- The total density in each cell, and the density of individual materials.

Other variables may be written to the NetCDF file. Although they might not be used by SPECT3D in the simulation, they can be viewed using the graphics in SPECT3D. Multiple time steps can be written in a single file.

Prism has developed and supplied algorithms for writing NetCDF output to Voss Scientific. These routines have been implemented in LSP.

Support for Post-Processing Large-Scale 2-D and 3-D Hydro/PIC Datasets

A substantial effort has been made to upgrade SPECT3D to support post-processing of results from large-scale 2-D and 3-D simulations of HEDP plasmas. Under a separate project, upgrades have been made to support calculations for 2-D and 3-D AMR (Adaptive Mesh Refinement) grids. We have also made upgrades to support post-processing of large-scale hydro/PIC simulation code datasets (containing ~ 10^7 - 10^8 volume elements). The upgrades that were made also provide the ability to perform SPECT3D post-processing large-scale calculations on single processor platforms, which facilitates developing a better understanding of the radiation physics processes (emission and absorption processes) in large-scale simulations.

Upgrades made to SPECT3D include the following:

- The hydro data (NetCDF) reader was updated in order to be able to select a subset of the volume elements in the hydro grid. Previously, for a given simulation time, all volume elements contained in a hydro data file were read in by SPECT3D and processed.
- New algorithms for calculating the intersection of lines-of-sight (LOSs) originating from the detector and passing through the hydro grid were developed. Previously, the entire grid in SPECT3D was set up, which included all volume element nodes and walls, and the identification of adjacent volume elements. While this approach has been shown to be very efficient for small-to-moderate-size grids (with < 10^6 volume elements), it became very inefficient for grids with > 10^7 volume elements. For hydro grids with a very large number of volume elements ($\gtrsim 10^7$), the new algorithms can result in an order of magnitude improvement in efficiency in computing LOS-grid intersections.
- Upgrades were made so that the results of LOS-grid intersection calculations are cached to avoid re-computation of intersections. This typically results in a reduction of a factor of 3 in CPU requirements.

As an example, the above upgrades will allow for the post-processing of LSP simulations of colliding jets, which is an inherently 3-D problem.

10. Polarization Spectroscopy Modeling Development

In an effort led by R. Mancini and P. Hakel at the University of Nevada-Reno (UNR), UNR has worked on extending the POLAR code to consider the population kinetics of magnetic sublevels in four consecutive ionization stages simultaneously and self-consistently, and on calculating autoionization and electron capture rates for magnetic sublevels. POLAR [24] is a code that computes time-dependent collisional-radiative atomic kinetics for magnetic sublevels in plasmas with anisotropic electron distribution functions. Magnetic sublevel populations are then used to calculate polarization dependent x-ray line emission intensities. Polarized line emission can be used as a diagnostic marker of anisotropy in the plasma.

As part of the input to POLAR, the code reads a set of input files with magnetic sublevel cross section and rate information. It is convenient to develop and test good approximations for autoionization and electron capture rates in order to readily compute this input data for POLAR. The approximation relies on the fact that in many cases autoionization has several channels to proceed but only one of them is the dominant or leading channel. Under these conditions, a simple formula can be worked out for the magnetic sublevel autoionization and electron capture rates similar to the equivalent result for magnetic sublevel spontaneous radiative decay. This approximation was tested and compared with complete calculations. The results indicate the usefulness of this approximation.

UNR pursued the investigation of opacity effects on polarized line emissions as possible signatures of plasma anisotropy. Work in this area had previously been performed mostly for astrophysical applications and has not been well known in our community. We therefore resolved to bridge this gap and provide the theoretical foundation of modeling of opacity effects on polarized line emissions that would be well-suited for researchers in the area of HEDP plasmas.

We based our approach on previous work in this area. In the past, we have separately modeled: (1) polarized line emissions in the optically thin approximation [25-26]; and (2) the opacity effects on unpolarized emission lines [27-29]. In this work, we combined elements of both efforts and arrived at a formalism that allows the post-processing of magnetic-sublevel atomic kinetics calculations with a radiation-transport model adapted to describe the evolution of all four Stokes parameters needed to characterize polarized radiation. In the process, we derived generalized formulae for emissivities and opacities for individual Stokes parameters in terms of magnetic-sublevel populations and multipole radiation fields. This work was presented as a contributed poster paper at the 2008 APS meeting and as an invited oral paper at the 2009 APIP meeting. Both conference appearances were followed by publications [30,31].

After developing the formalism, we performed modeling studies of the effects that opacity can have on the polarization degree of two selected lines in He-like Cl. The first line is the He-alpha line whose lower level has J=0 and hence a single magnetic sublevel. The second line is a satellite of the Ly-α whose lower level has three magnetic sublevels since its J=1. Unlike the ground state of the He-like ion, this J=1 level can support

alignment because its sublevels can be unequally populated under anisotropic plasma conditions. This opens the possibility that the intrinsic polarization degree of this line (*i.e.*, the polarization that would be observed if the plasma were optically thin) could be altered during radiation transport. This is confirmed by our modeling results shown in Figures 10.1 and 10.2 (the solid black trace). The polarization of the He- α line is unaffected by the radiation transport of its self-emission. The Ly- α satellite, on the other hand, changes value between the optically thin and thick limits. This is a consequence of different opacity values for the two polarized components, which is caused by the alignment in the lower level of the Ly- α satellite. In addition, we also studied the effect of an unpolarized backlighter on line polarization (colored dashed traces). Here, the solution of the polarization-state-dependent radiation transport equation shows the reduction of the polarization degree of the optically thin case in proportion to the increasing intensity of the backlighter relative to the plasma self-emission. The optically thick limit is unaffected, however. Both of these results are intuitively understandable and show that the method provides a reasonable account of opacity effects on polarized radiation.

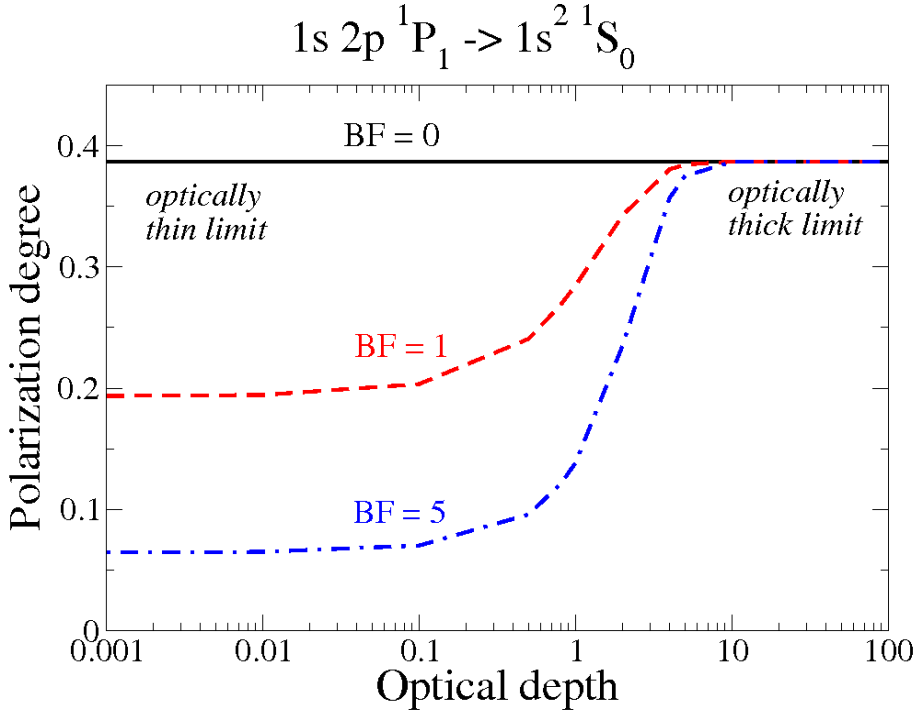

Figure 10.1. Polarization of the He-α line for $n_e = 10^{22}$ cm^{-3}, $T_e = 500$ eV, $T_h = 1$ keV, $\alpha = 0.2$.

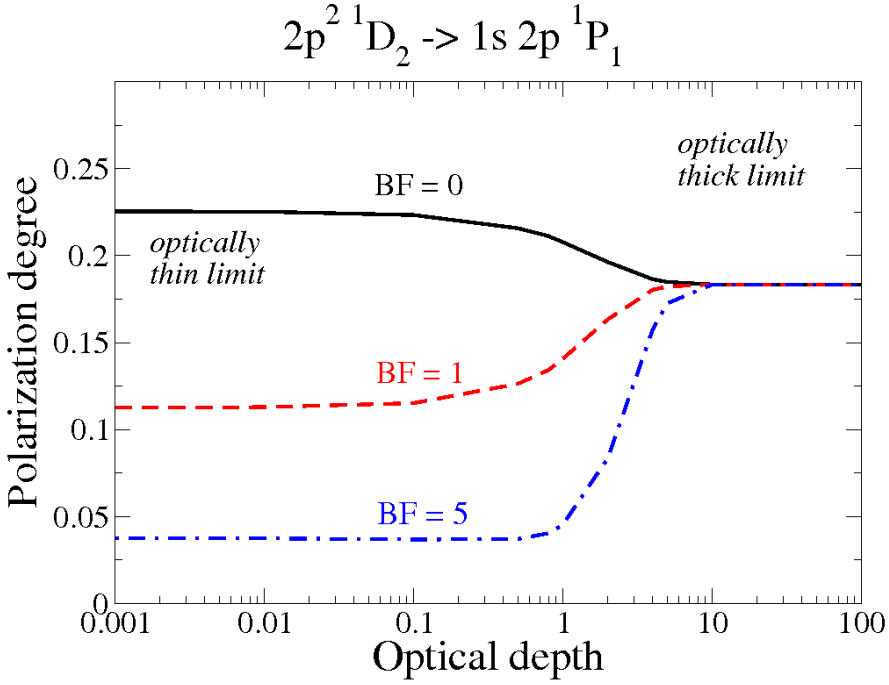

Figure 10.2. Polarization of the Ly-α line for $n_e = 10^{22}$ cm^{-3}, $T_e = 500$ eV, $T_h = 1$ keV, $\alpha = 0.2$.

To date, we have provided a rather general formalism for constructing the radiation transport equation for the Stokes parameters and using it to post-process the results of magnetic-sublevel atomic kinetics models of an anisotropic plasma. Future work will focus on improving the magnetic-sublevel atomic kinetics component of the model, notably the calculation of rates of collisionally-driven processes using arbitrary electron distribution functions.

11. Technical Papers and Presentations

The following technical papers and presentation were made during the course of this project:

- "SPECT3D – A Multi-Dimensional Collisional-Radiative Code for Generating Diagnostic Signatures Based on Hydrodynamics and PIC Simulation Output", J. J. MacFarlane, I. E. Golovkin, P. Wang, P. R. Woodruff, and N. Pereyra, *High Energy Density Physics* **3**, 181 (2007).
- "SPECT3D Post-Processing of LSP PIC Simulations: Application to Short-Pulse Laser Experiments", J. J. MacFarlane, P. Wang, I. E. Golovkin, P. R. Woodruff, N. Pereyra, R. C. Mancini, D. Welch, and T. Hughes, American Physical Society Division of Plasma Physics Meeting, Philadelphia, PA, November 2006.
- "Development and Benchmarking of Radiation Transport Models in LSP", I. E. Golovkin, J. J. MacFarlane, P. R. Woodruff, P. Hakel, R. C. Mancini, T. Hughes, D. Welch, C. Thoma, F. D. Witherspoon, M. Phillips, I. N. Bogatu, J.-S. Kim and S. Galkin, American Physical Society Division of Plasma Physics Meeting, Orlando, FL, November 2007.
- "Inclusion of Radiation Transport and EOS Ionization Tables in Hybrid-PIC Simulations of Plasma Jets", P. Hakel, R. Clark, T. Hughes, C. Mostrom, I. E. Golovkin, P. R. Woodruff, and J. J. MacFarlane, American Physical Society Division of Plasma Physics Meeting, Orlando, FL, November 2007.
- "EMHD Calculations of Plasma Jet Acceleration", T. Hughes, C. Thoma, J.-S. Kim, and S. Galkin, American Physical Society Division of Plasma Physics Meeting, Orlando, FL, November 2007.
- "Opacity Effects on the Polarization of Line Emissions in Astrophysical Plasmas," P. Hakel and R. C. Mancini, *Astrophys. Space Sci.*, in press (2009).
- "Polarization Spectroscopy Modeling with the Inclusion of Radiation Transport," P. Hakel, R. C. Mancini, and Y. Sentoku, in preparation.

12. Summary

In this project, we have developed and implemented advanced radiation physics modeling into the LSP hybrid PIC-fluid code. The improved modeling includes: (1) multi-dimensional, multi-frequency radiation diffusion modeling; (2) updated energy equation modeling that more accurately computes plasma temperatures based on realistic equations of state; (3) better interfacing with SPECT3D that will allow for generating images and spectra based on LSP simulation results. In addition, we have performed radiation physics simulations to examine the effects of radiation cooling in plasma jet experiments, and the effects of small amounts of contaminant from the electrode on radiation cooling. The SPECT3D code has also been updated to better support post-processing simulation code output with large-scale 2-D and 3-D datasets, which will eventually be required for simulating plasma jets in complex geometrical configurations (*e.g.*, colliding jets).

The work performed under this project has led to significant improvements in the modeling capabilities of the LSP and SPECT3D simulation codes. In the future, it will be important to build on this these efforts and apply these codes in the study of DOE-sponsored high energy density physics (HEDP) experiments, such as the study of plasma jets and fast ignition physics.

References

1. D. R. Welch, D. V. Rose, B. V. Oliver, and R. E. Clark, *Nucl. Instrum. & Methods Phys. Res. A* **464**, 134 (2001).
2. T. P. Hughes, S. S. Yu, and R. E. Clark, *Phys. Rev. ST-AB* **2**, 110401 (1991).
3. J. J. MacFarlane, I. E. Golovkin, and P. R. Woodruff, *J. Quant. Spectrosc. Rad. Trans*. **99**, 381 (2006). A discussion of PROPACEOS appears in the appendix of this paper.
4. J. J. MacFarlane, I. E. Golovkin, P. R. Woodruff, P. Wang, and N. A. Pereyra, *High Energy Dens. Phys*. **3**, 181 (2007).
5. T. Hughes, T. Genoni, R. Clark, D. Welch, M. Phillips, and D. Witherspoon, "*Simulation of Plasma Jet Dynamics Using Hybrid Particle-in-Cell Methods*", Bull. Am. Phys. Soc. **51**, 322 (Oct. 2006).
6. D. R. Welch, D. V. Rose, M. E. Cuneo, R. B. Campbell, and T. A. Mehlhorn, *Phys. Plasmas* **13**, 063105 (2006).
7. R. M. More *et al*., *Phys. Fluids* **31**, 3059 (1988).
8. Y. T. Lee and R. M. More. *Phys. Fluids* **27**, 1273 (1984); M. P. Desjarlais, *Contrib. Plasma Phys*. **41**, 267 (2001).
9. S. I. Braginskii. Transport processes in a plasma. In *Reviews of Plasma Physics*, Volume 1, p. 205, Plenum, New York, 1965.
10. M. L. Alme, and J. R. Wilson, *Astrophys. J.* **194**, 147 (1974).
11. C. D. Levermore, and G. C. Pomraning, *Astrophys. J.* **248**, 321 (1981).
12. D. S. Kershaw, *Comp. Physics* **39**, 375 (1981).
13. G. A. Moses, and J. Yuan, University of Wisconsin Fusion Technology Report UWFDM-1213, Madison, WI (2005).
14. T. A. Brunner, Sandia National Laboratories Report SAND2002-1778, Albuquerque, NM (2002).
15. N. J. Turner, and J. M. Stone, *Astrophys. J. Suppl. Ser*. **135**, 97 (2001).
16. J. E. Morel, *et al*., *Comp. Physics* **144**, 17 (1998).
17. Mihalas, D., Stellar Atmospheres, Second Edition (Freeman, New York, 2008).
18. NIST Atomic Spectra Database, Ver 3.1, see: http://www.physics.nist.gov/PhysRefData/ASD/index.html.
19. P. Wang, Ph.D. Dissertation, Dept. of Nuclear Engineering and Engineering Physics, University of Wisconsin, Madison, WI (1991).
20. J. Abdallah, Jr. and R. E. H. Clark, Los Alamos National Laboratory Report LA-10454, Los Alamos, NM (1985).
21. C. A. Iglesias and F. J. Rogers, *Astrophys. J*. **371**, L73 (1991). C. A. Iglesias and F. J. Rogers, *Astrophys. J*. **464**, 943 (1996).
22. J. E. Bailey, G. A. Rochau, C. A. Iglesias, J. Abdallah, Jr., J. J. MacFarlane, I. Golovkin, P. Wang,4 R. C. Mancini, P.W. Lake, T. C. Moore, M. Bump, O. Garcia, and S. Mazevet, Phys. Rev. Lett. **99**, 265002 (2007).

23. Information on NetCDF can be found at: http://www.unidata.ucar.edu/software/netcdf

24. P. Hakel, R. C. Mancini, J. C. Gauthier, E. Minguez, J. Dubau, and M. Cornille, *Phys. Rev. E* **69**, 056405 (2004).

25. Hakel, P., et al., 2007. Phys. Rev. A 76, 012716.

26. Hakel, P., et al., 2009. J. Phys. B: At. Mol. Opt. Phys. 42, 085701.

27. Andiel, U., et al., 2002. Europhys. Lett. 60 (6), 861.

28. Andiel, U., et al., 2002. J. Mod. Opt. 49 (14/15), 2615.

29. Eidmann, K., et al., 2003. J. Quant. Spect. Rad. Transf. 81, 133.

30. Hakel, P. and Mancini, R. C., 2009. Astrophys. Space Sci. 322 (1-4), 113.

31. Hakel, P., et al., submitted to the proceedings of the 16th Atomic Processes in Plasmas Conference, Monterey, California, 2009.